An active pixel-matrix electrocaloric device for targeted and differential thermal management

*Peijia Bai, Quan Zhang, Heng Cui, Yiwen Bo, Ding Zhang, Wen He, Yongsheng Chen, Rujun Ma**

P. Bai, Dr. Q. Zhang, H. Cui, Y. Bo, Dr. D. Zhang, Dr. W. He, Prof. R. Ma

School of Materials Science and Engineering, National Institute for Advanced Materials, Smart Sensing Interdisciplinary Science Center, Nankai University, Tianjin, 300350, P. R. China.

Email: malab@nankai.edu.cn

Prof. Y. Chen

State Key Laboratory and Institute of Elemento-Organic Chemistry, Centre of Nanoscale Science and Technology and Key Laboratory of Functional Polymer Materials, College of Chemistry, Nankai University, Tianjin, 300071, P. R. China.

Keywords: Electrocaloric effect, Electrostatic actuation, Targeted thermal management, Solid-state cooling

This article has been accepted for publication and undergone full peer review but has not been through the copyediting, typesetting, pagination and proofreading process, which may lead to differences between this version and the Version of Record. Please cite this article as doi: 10.1002/adma.202209181.

More than 55% of electronic failures are caused by damage from localized overheating. Up to now, there is still no efficient method for targeted temperature control against localized overheating. Although some existing thermal management devices handle this issue by full coverage cooling, it generates a lot of useless energy consumption. Here, we report a highly efficient pixel-matrix electrocaloric (EC) cooling device, which can realize a targeted and differential thermal management. The modified P(VDF-TrFE-CFE) reaches a large adiabatic temperature change of 7.8 K and is more suitable for thermal transfer and electrostatic actuation at high frequencies. All active pixels in the EC cooling device exhibit a stable temperature span of 4.6 K and a heat flux of 62 mW/cm^2, which is more than twice that of the one-layer EC device. Each refrigeration pixel can be independently controlled and effectively cool down the localized overheating site(s) in situ. The surface temperature of the simulated CPU decreased by 33.2 K at 120 s after applying this EC device. Such a compact, embeddable, low cost and active solid-state pixel-matrix cooling device have a great potential for localized overheating protection in microelectronics.

1. Introduction

In recent years, miniature integrated circuits and electronic chips have become an important component of technological progress.[1-4] With the continued improvement of the integration of electronic chips and circuits, the total power consumption has risen exponentially, and electronics failure will become increasingly prominent. Before the Central Processing Unit (CPU) moved into multi-core, coolers can deal with the chip as a single-site heat source for effective cooling. But the multi-core CPU is packaged as a whole, and the localized overheating site in one core can heat others up. The localized overheating site makes the thermal challenge much more difficult, and it caused more than 55% of all failures in current electronics. [6] As operating temperature approaches 70-80 °C, the performance of electronics will degrade by ~10% for every 2 °C increase.[7] So, the precise cooling technology in integrated circuits has become increasingly a restrictive factor affecting the development of the electronics industry.[8-10] Vapor-compression refrigeration systems are bulky, complex and difficult to scale down to meet the cooling demands of electronic chips. Existing refrigerants also have high global warming potentials, and present an environmental risk upon leakages or improper disposal. Therefore, it is urgent and vital to develop a highly efficient, environmentally friendly, compact, and portable refrigeration device to achieve precise cooling.

Solid-state cooling systems, especially caloric-effect-based refrigeration such as the elasto/baro caloric effect,[11] magnetocaloric effect,[12] and electrocaloric (EC) effect,[8,9,13-15] have the advantages of no compressors and conventional liquid or vapor refrigerants, environmental protection, and rapid cooling. The EC refrigeration has been praised for its high coefficient of performance (COP), simple setup, low cost, and feasibility for embedded application in compact integrated circuits.[13] Thus, they can solve the practical cooling requirements of integrated microelectronics that traditional compressor technology is difficult to address. The EC is a reversible adiabatic temperature change (ΔT) and/or isothermal entropy change (ΔS) in dielectric materials induced by an external electric field change (ΔE).[8] Although a large voltage is applied, the generated current and corresponding power consumption are still very small, because of the insulating properties of the EC materials. Therefore, EC refrigeration device exhibits a great application prospect in miniature electronics cooling.

Compared to the inherent brittleness of EC multilayer ceramic capacitors,[16,17] the poly(vinylidene fluoride) (PVDF)-based ferroelectric polymers have been praised for their light weight, large isothermal entropy change, flexibility, and low-temperature processing conditions.[18] The poly(vinylidene fluoride-tertrifluoroethylene-chlorofluoroethylene) [P(VDF-TrFE-CFE)] is suitable for microelectronic cooling due to its high calculated isothermal entropy change of 55 J (kg·K)$^{-1}$ and large adiabatic temperature change of 12 K.[8] In addition, various studies to improve EC performance have been carried out. PVDF terpolymers modified with triethylamine (Et_3N) to form double bonds (DB) within the backbone could significantly improve EC performance.[19,20] Nanocomposites comprised of PVDF terpolymer with $Ba_xSr_{1-x}TiO_3$,[21-23] $(1-x)Pb(Mg_{1/3}Nb_{2/3})O_3$-$x$$PbTiO_3$,[24] $BaZr_{0.21}Ti_{0.79}O_3$ nanofibers,[25,26] and graphene[27] have also been reported with enhanced EC properties. Even though numerous studies have reported effective EC performance enhancements, few pixel-matrix EC cooling devices with in situ temperature control and active precise cooling have been actually investigated. Single-unit, double-unit and cascade EC devices based on PVDF terpolymers have demonstrated high cooling performance, and played a good role in cooling lithium battery and CPU. [13-15] However, among the reported EC cooling devices, the temperature of different hot spots on the electronic devices cannot be precisely controlled to solve the critical problem of localized overheating of electronic chips.

Here, we demonstrated a highly efficient and precise pixel-matrix cooling device based on P(VDF-TrFE-CFE) nanocomposites, which could actively control/cool the overheating site(s) as needed in situ. Through chemical modification with triethylamine (Et_3N), double bonds were introduced along the P(VDF-TrFE-CFE) backbone, which lowered the energy barrier for dipole flipping and enhanced the EC performance. In addition, the EC performance of the pixel-matrix EC film was further improved by doping $Ba_{0.6}Sr_{0.4}TiO_3$ nanoparticles (BST NPs), and the maximum adiabatic temperature change (ΔT) reached 7.8 K at 110 MV/m. Importantly, we focused on improving the stability for thermal conduction and electrostatic actuation at high frequencies. The pixel-matrix EC polymer stack did not show any sign of electrical failure or other damage after 1750 cycles of charging-discharging.

Moreover, the EC device with a 3×3 pixel-matrix achieved a large temperature span of 4.6 K. Each refrigeration pixel on the pixel-matrix EC cooling device can be independently controlled, and can automatically, precisely and effectively cool down the localized overheating site(s) on the electronic chip as needed. The surface temperature of the simulated CPU was 33.2 K lower than that of the CPU cooled in air after applying the EC cooling device. Thus, this pixel-matrix EC cooling device with high efficiency and automatic response provides a new strategy for localized overheating in miniature electronics.

2. Results and discussion

Figure 1a shows schematic diagram of the de-hydrochlorination process to form double bonds in P(VDF-TrFE-CFE). The de-hydrochlorination occurs via nucleophilic attack on the CFE sequence by triethylamine to form DB as described in Figure S1. The content of DB is easily controlled by the content of Et_3N, reaction time and temperature.[19,20] Figure 1b displays the fabrication steps for the EC double-stack with a 3×3 pixel-matrix electrodes (See Experimental Section for details). Briefly, pre-dissolved solution was drop-casted onto a glass substrate, followed by heating at 100 °C for 2h to completely evaporate the solvent. After peeling off the film from the glass substrate, a dispersion of carbon nanotubes (CNT) was spray-coated onto the EC film by the pre-designed 3×3 pixels structure to form the pixel-matrix electrodes (6.5 mm × 6.5 mm). Then, one of the as-prepared films was laminated directly on top of another with only a group of CNT pixel-matrix electrodes sandwiched between the EC films by hot pressing at 125 °C. The bottom surface of the stack was also spray-coated with CNT pixel-matrix electrodes to complete the fabrication of a two-layer EC stack. Finally, the EC laminate was annealed in a vacuum oven at 120 °C for 500 min to increase the crystallinity.[28]

Figure 1c exhibits the X-Ray powder diffraction pattern of the BST NPs. There is no obvious additional diffraction peak in the XRD patterns compared with the standard diffraction spectrum of JCPDS Card No:89–2475, which indicates that the synthesized BST NPs have high purity without any secondary phase. TEM image shows that the BST NPs have a high crystallinity with a size between 10-20 nm which is smaller than previously reported. [22] From the cross-sectional morphology, a clear boundary between two EC layers can be observed, and each layer has a similar thickness of 33 μm (Figure 1d). Moreover, the BST NPs were well dispersed in the DB-modified P(VDF-TrFE-CFE) matrix (inset in Figure 1d and Figure S2). The photograph of the EC double stack exhibits canary yellow with good flexibility as shown in Figure 1e. Figure 1f shows the schematic side view of EC double stack, where the embedded middle CNT pixel-matrix electrodes of the stack is the anode and the two outer CNT pixel-matrix electrodes are the cathodes.

^{1}H NMR spectra of DB-modified P(VDF-TrFE-CFE) show that a small amount of DB is introduced into P(VDF-TrFE-CFE) molecular chains after de-hydrochlorination treatment (**Figure 2**a). The content of DB in carbon chains of P(VDF-TrFE-CFE) molecules increases from 0 ‰ to 10.5 ‰ with the increase of Et_3N content in reaction solution (Table S1). The introduction of DB reduces the lamellar crystal thickness,[29] resulting in a lower energy barrier for dipole flipping.[30] This is conductive to improve EC performance of P(VDF-TrFE-CFE) by increasing its polarization.[19] Figure 2b and c show P-E loops of modified P(VDF-TrFE-CFE) with different contents of DB at 10 Hz. The maximum polarization increases from 0.054 C/m^2 for pure terpolymer to 0.075 C/m^2 for 7.1‰ of DB-modified P(VDF-TrFE-CFE) (DB 7.1), and gradually decreases with the further increase of DB content. The dielectric spectra exhibit that the P(VDF-TrFE-CFE) modified with a small content of DB has a small dielectric loss.[19] ΔT of P(VDF-TrFE-CFE) film under different electric fields is directly measured by an infrared camera. Besides CNT, the electrodes also can be composed using metal materials such as gold, silver, and copper, according to the functional requirements. In order to collect real temperature change data, the infrared emissivity of the corresponding electrodes should be calibrated in advance to avoid likely mismeasurement (Figure S3-5 and Table S2). As shown in Figure 2d, the temperature drop of modified P(VDF-TrFE-CFE) gradually increases with the increase of electric field from 40 MV/m to 160 MV/m. Under the same electric field, the temperature drop always increases first and then decreases with the increase of DB content in P(VDF-TrFE-CFE). The variation of temperature drop with DB content is consistent with that of maximum polarization. The maximum improvement of EC performance is achieved when the content of DB is 7.1 ‰. These results show that DB 7.1 has a maximum temperature drop of 6.5 K under electric field of 160 MV/m.

Even though numerous studies of adding nanocomposites have reported effective EC performance enhancements, most of them are not suitable for fabricating EC cooling devices due to the increase in dielectric loss and the decrease in breakdown strength of materials. In this work, smaller size BST NPs (10-20 nm) were synthesized as fillers to reduce agglomeration and avoid large dielectric losses. The incorporation of BST NPs can further improve EC performance of DB 7.1, but the introduction of excessive amounts can decrease the breakdown strength of nanocomposite (Figure S6 and Table S3). Among them, the modified P(VDF-TrFE-CFE) doped with 15 wt% BST NPs (DB 7.1@BST-15) has larger temperature drop. This is related to the formation of the BST NPs percolation network in modified P(VDF-TrFE-CFE) matrix.[21,31,32] Benefitted from synergy between DB modification and BST NP doping, DB 7.1@BST-15 exhibits an optimal improvement in EC performance (Figure S7-9). In addition, BST NPs in the polymer significantly contributed to the improvement of both Young's modulus and thermal conductivity of P(VDF-TrFE-CFE) (**Figure 3**a).[31,33] The moderately enhanced Young's modulus attenuates the electro-strictive behavior of polymer nanocomposite. Moreover, the improved thermal conductivity can accelerate the heat exchange between the EC stack and the heat source or heat sink, which helps to construct the cooling device and also increases the temperature span of the cascade device.[34,35] Therefore, DB 7.1@BST-15 was chosen to further fabricate two-layer EC nanocomposite stack. When the electric field is applied in the air, a small amount of heat in the EC stack is rapidly transferred to the air through its surface by radiation and conduction. This results in the temperature change of the EC stack measured by the infrared camera being smaller than its actual temperature change. In addition, the total heat increases with the thickness of the EC stack, while the heat transfer to the environment via the stack surface remains essentially constant. When measured with an infrared camera in the air, the thicker stack has a higher temperature change than a thinner stack under the same electric field (Figure S10). Moreover, different components of VDF:TrFE:CFE lead to different temperature change. Even for the same component, the temperature change of P(VDF-TrFE-CFE) varies when measured at different ambient temperatures, as shown in Table S4.

Compared with two-layer stack prepared by pure P(VDF-TrFE-CFE), the two-layer EC nanocomposite stack consistently exhibits higher temperature drop under the same electric field. When the electric field is 110 MV/m, the temperature drop of two-layer EC nanocomposite stack is 7.8 K, 56% higher than that of pure P(VDF-TrFE-CFE) stack (Figure 3b). The temperature of the stack reversibly rises and drops with the alternating charging and discharging. With the increase of frequency of the charging-discharging process, the temperature change only decreases slightly (Figure 3c). This is because the high-voltage power supply cannot completely remove the electric field in time, so that the dipoles cannot return to their original state. However, the two-layer EC nanocomposite stack shows an outstanding robustness of EC performance. For example, after 1750 charging-discharging cycles with an applied electric field of 60 MV/m and frequency of 1 Hz, the temperature drop is kept the same as before (Figure 3d).

Figure 4a shows the schematic illustration of a pixel-matrix EC cooling device based on a two-layer EC nanocomposite stack. From top to bottom, it involves CNT electrode, polyimide insulating film, PDMS spacer, two-layer EC nanocomposite stack, polyimide insulating film and aluminum plate (used as heat sink). By pre-depositing pixel-matrix CNT electrode pairs in each modified P(VDF-TrFE-CFE) nanocomposite film, the active pixels are successfully integrated into a two-layer EC stack. As shown in Figure 4b, the infrared images record the instantaneous temperature rise and drop of the EC stack with a 3 × 3 electrode matrix, when an electric field is applied (left) and removed (right), respectively. The extent of active pixels is determined by the size of corresponding electrode pairs. This means that these active pixels could be activated individually or together in different combinations by applying or removing electric field to realize the goal of targeted thermal management. Taking an active pixel as an example, a sudden temperature rise of 4.5 K appears once applying an electric field of 60 MV/m in 1 ms (Figure 4c). Then, the temperature of the active pixel could be reduced to the room temperature under this constant electric field due to the heat transfer from the active pixel to the air. While removing this electric field, the temperature shows an opposite evolution process. All active pixels are a typical temperature change behavior of the charging-discharging process, which is independent of the shape, size, and number of electrode pairs in the EC stack. Therefore, if the temperature of each site/local spot is input as a trigger into our device, easily in the targeted microelectronics, then this thermal management system could respond automatically to temperature control at an accurate size level.

A control circuit is designed to precisely control the movement of EC stack between heat source and heat sink, as well as the repeated charging-discharging process for EC effect. Ideally, EC stack is expected to release heat to the heat sink while in contact with the heat sink, and cool down to absorb heat from the heat source when in contact with the heat source (Figure 4d). In this way, the heat will be efficiently transferred from the heat source to the heat sink. More detailed cooling device structure and system operation principles have been described in the previous reports[13, 15] and Figure S11. By changing the combination of active pixels in the EC stack, the morphology and temperature distribution of the cool region in the EC cooling device could be freely adjusted (Figure 4e and Video 1).

Figure 4f shows the stable temperature span of pixel-matrix EC cooling device under electric field of 60 MV/m at a frequency of 2 Hz. Operation frequency is an important parameter that affects the cooling power of our EC cooling device. The temperature span decreases slightly with the increase of frequency, which is consistent with the results in Figure 3c. Importantly, our cooling device is able to operate over a broad frequency range as needed (Video 2). For low frequency, excessive heat loss from air convection weakens the cooling effect. And for high frequency, the pixel-matrix EC cooling device exhibits a saturated cooling power, which is mainly limited by the heat transfer capability between EC nanocomposite stack and heat source (or heat sink). The comparison of average heat flux with this class of EC device is shown in Figure 4g. The average heat flux is measured to be 62 mW/cm^2, which exceeds two-layer EC cooling devices reported in the literature.[13-15] This is because the modified P(VDF-TrFE-CFE) improves EC performance and is more suitable for thermal conduction and electrostatic actuation at high frequencies. As the frequency increases, the heat flux of a single active pixel continues to increase and gradually trends to be saturated at a frequency higher than 1.5 Hz (Figure 4h). In addition, the total energy consumption of a single active pixel, including the EC effect and electrostatic actuation, increases with frequency (Figure S12). Obviously, the current shows a peak signal.[15] In order to ensure the accuracy of the current measurement, the larger active area (2×4 cm^2) EC polymer stack was measured (Figure S13) and showed the larger area of the current signal, which is related to the charging and discharging of the larger EC polymer capacitor. The current area of a single active pixel presents a spike shape due to the low charge content. The COP, the amount of heat removed per electrical energy consumed, is commonly used to evaluate the efficiency of cooling device. It descends as the energy consumption increases at a higher frequency. The average heat flux is measured to be 62 mW/cm^2 with a COP of 10.4 under the electric field of 60 MV/m at the frequency of 1.5 Hz (Figure S14-15). Our EC cooling device shows a stable temperature span of 4.6 K at an electric field of 60 MV/m (Figure 4f and Figure S16), which exceeds all such class of single-unit EC cooling devices. This is benefited from the huge improvement in EC performance and thermal conductivity of our modified EC materials.

For localized overheating CPU, our pixel-matrix EC cooling device provides a targeted and differentiated thermal management strategy for flexible temperature control (**Figure 5**a and b). During the whole operation process, two-layer EC nanocomposite stack is continuously traversed between the heat source and the heat sink by an alternating electrostatic force. For localized overheating, the pixel-matrix EC cooling device can choose to wake up active pixels corresponding to different hot spots. The activation of the active pixel depends on whether the electric field for EC effect is applied to its electrode pair, and the cooling power of active pixel is controlled by adjusting the applied electric field according to the level of overheating. A simulated CPU composed by separated ceramic heating plates (NO:CT-JRP, 5V/2W) with 3 × 3 pixels is fabricated (Figure 5a, Figure S17). Figure S18 shows the heat flux curves of simulated CPU with different power. By applying different Joule heating power, the localized overheating scene is created. Among them, the temperature of pixel ③, ⑤ and ⑨ is 81.0 °C, 90.5 °C, and 72.0 °C, respectively (Figure 5c). Meanwhile, three corresponding active pixels in the pixel-matrix EC cooling device are activated simultaneously to realize active and accurate cooling of different hot spots. In addition, we compared the cooling performance of our pixel-matrix EC cooling device with two commercial fans in a simulated scene. A high-precision thermocouple connected to a recorder is attached to the simulated CPU surface to accurately record the temperature in time (Figure 5d, Figure S19). When a constant heating power is applied, the surface temperature of the simulated CPU exposed in air rapidly rises from room temperature to 93.3 °C within 120 s (The thermocouple is attached to the surface of the simulated CPU by thermal conductive silicon). A desk fan (GFD-6KL, 5V, 0.5A, 2.5W) is placed 5 cm above the simulated CPU, and the surface temperature of the CPU drops from 93.3 to 77.7 °C. The CPU air cooler (DELTA-AFB0705HB, 5V, 0.2A, 1W) consists of an aluminum block and a mini fan, which is directly removed from the computer. The surface temperature of the CPU drops rapidly from 93.3 to 57.3 °C after applying CPU air cooler, this is because the efficiency of solid-solid heat transfer is much greater than that of air convection cooling. Under the same conditions, our EC cooling device (Energy consumption of 7.85 mW) operating at full power is able to consistently suppress the temperature of the simulated CPU around 59.1 °C. As a reference, the surface temperature of simulated CPU is about 71.6 °C at 120 s, when the electric field for EC effect is turned off. Because the heat of simulated CPU is efficiently transferred to the heat sink (3 mm aluminum block). The EC device showed better cooling capacity than the CPU air cooler at less than 40 °C, because the relaxor P(VDF-TrFE-CFE) worked effectively in this temperature range. Overall, these comparison results show that our pixel-matrix EC cooling device is comparable to the CPU air cooler in cooling performance, and far superior to mini desk fan. Furthermore, the compact structure is not available with the above two commercial cooling solutions.

3. Conclusion

In summary, we demonstrated a pixel-matrix EC cooling device driven by electrostatic force. The modified P(VDF-TrFE-CFE) in accompanying enhancement of Young's modulus and thermal conductivity makes more suitable for thermal conduction and electrostatic actuation at high frequencies. At room temperature, two-layer EC nanocomposite stack exhibits a large temperature change of 7.8 K under electric field of 110 MV/m, and there is no obvious degradation of EC performance even after 1750 charging-discharging cycles. The pixel-matrix EC cooling device based on two-layer EC nanocomposite stack could achieve a larger temperature span of 4.6 K under lower electric field of 60 MV/m, exceeding all single-unit EC devices reported in the literature. Each refrigeration pixel on the pixel-matrix EC cooling device can be independently controlled, and can precisely and effectively cool down the hot spots of different positions and heat on the electronic chip. The surface temperature of the simulated CPU dropped 33.2 K after applying this pixel-matrix EC device, which is comparable to the commercial CPU air cooler and far superior to the desk fan. Such a compact, low-energy, high-performance, pixel-matrix EC cooling device offers a targeted and differential thermal management strategy, and has a wide application prospect for overheating protection of microelectronics.

4. Experimental Section

Chemical modification of P(VDF-TrFE-CFE): 0.5 g of pure P(VDF-TrFE-CFE) (64.8/27.4/7.8mol%, Piezotech Arkema) was completely dissolved in 10 ml of dimethyl sulfoxide (Aladdin, AR, 99.9%) by stirring at room temperature. Then, triethylamine was added into solution, which was further stirred continuously at 40 °C for 5 h. The product was precipitated in water, collected, and dried at 60 °C in a vacuum. After that, the dried precipitate was dissolved in acetone and re-precipitated in a 40 vol% of ethanol aqueous solution. Finally, the polymer was collected and dried at 80 °C in a vacuum.

Synthesis of $Ba_{0.6}Sr_{0.4}TiO_3$ nanoparticles (BST NPs): Cubic BST NPs were prepared by hydrothermal reaction. $BaCl_2 \cdot 2H_2O$ (Xiya reagent, AR, 99.9%) and $SrCl_2 \cdot 6H_2O$ (Xiya reagent, AR, 99.9%) were dissolved into 60 mL of KOH (Meryer, ACS) aqueous solution with a concentration of 1.2 mol/L. The molar ratio between Ba and Sr is 6:4. Meanwhile, 2.04 mL tetrabutyl titanate (Strem Chemicals, AR, 99.9%), 15 mL oleic acid (Meryer, AR, 99.9%), 60 mL n-butanol (Aladdin, AR, 99.9%), and 15.6 µL oleic amine (surfactant, Aladdin, AR, 99.9%) were mixed uniformly. Then, the above solutions were mixed in a sealed Teflon-lined stainless-steel autoclave and heated at 135 °C for 18 h. The precipitation was washed sequentially with acetone, 5 wt% acetic acid and ethanol. The final product was dried at 60 °C in a vacuum.

Fabrication of two-layer EC nanocomposite stack: Modified P(VDF-TrFE-CFE) was dissolved in N, N-Dimethylformamide (DMF, Aladdin, AR, 99.9%) at a concentration of 10 wt% and filtered using a 0.22 µm PTFE filter. Meanwhile, BST NPs were dispersed in DMF by tip ultrasonic. Then, the filtered modified P(VDF-TrFE-CFE) solution and BST NPs dispersion were mixed by tip ultrasonic for 1.5 h and stirred for 3 h as the precursor of EC nanocomposite film. The EC nanocomposite film was prepared by casting precursor on a glass plate and heating at 100 °C for 2 h. After the solvent has completely evaporated, the film was peeled off from the glass plate and annealed at 120 °C for 500 min in a vacuum. Carbon nanotubes (CNT, XFNANO, carboxylic single-walled carbon nanotube, purity >90 %, 1-2 nm in diameter and 1-3 µm in length) conductive network as electrodes were deposited on the EC film by spray-coating (Dahua, DH350E). Two EC films were integrated to fabricated a two-layer EC nanocomposite stack by hot pressing at 125 °C.

Characterizations and measurements: X-ray diffraction data was obtained by X-ray powder diffraction instrument (Rigaku Smart Lab SE). The cross-sectional morphology was observed by using SEM (JEOL, JSM-7800). The polarization-electric field loops (P-E loops) were measured by a ferroelectric tester (Precision Premier Workstation, Radiant Technologies, USA). Infrared images and videos were captured by an infrared camera. High voltage was provided by a high-voltage power supply (Dongwen, DW-P103-0). The heat flux ($\Phi_{\text{heat flux}}$) was measured by heat flux sensor (Omega HFS-5).

Fabrication of precise fixed-point cooling Device: The array precise fixed-point cooling device was driven by the electrostatic actuation mechanism as described in Ref 13. The COP is calculated as $\mathrm{COP} = \frac{\Phi_{\text{heat flux}}}{W_{\text{electric energy consumption}}}$, where $\Phi_{\text{heat flux}}$ and $W_{\text{electric energy consumption}}$ are the total heat flux and the total electric energy consumption of EC device in one operation period, respectively. The heat flux ($\Phi_{\text{heat flux}}$) was measured by the heat flux sensor (Omega HFS-5). $W_{\text{electric energy consumption}} = \int_{t1}^{t2} V_{EC} \times I_{EC}\,dt$, where t1 and t2 are the start and the end time of an entire operation period, respectively, and V_{EC} and I_{EC} are the measured voltage and current, respectively (Figure S12).

Supporting Information

Supporting Information is available from the Wiley Online Library or from the author.

Acknowledgments

This work is supported by National Key R&D Program of China (Grant No. 2020YFA0711500 and 2020YFA0711501), and the National Natural Science Fund of China (51973095, 52273248).

Competing interests: The authors declare no competing interests.

References

[1] T. Wei, *Nature* **2020**, 585, 188.

[2] J. Shi, D. Han, Z. Li, L. Yang, S. Lu, Z. Zhong, J. Chen, Q. M. Zhang, X. Qian, *Joule* **2019**, 3, 1200.

[3] I. Di Bernardo, J. Hellerstedt, C. Liu, G. Akhgar, W. Wu, S. A. Yang, D. Culcer, S. K. Mo, S. Adam, M. T. Edmonds, M. S. Fuhrer, *Adv. Mater.* **2021**, 33, 2005897.

[4] Z. Yang, S. Shao, M. Fan, L. Yang, *Ecol. Ecol. Econ.* **2020**, 181, 106912.

[5] T. Q. Trung, N. E. Lee, *Adv. Mater.* **2017**, 29, 1603167.

[6] T. Gan, T. Ming, W. Fang, Y. Liu, L. Miao, K. Ren, M. H. Ahmadi, *J. Therm. Anal. Calorim.* **2019**, 141, 45.

[7] Z. Guo, *Adv. Appl. Mech.* **2000**, 30, 1. DOI: 10.6052/1000-0992-2000-1-J1998-001.

[8] B. P. Neese, B. Chu, S. Lu, Y. Wang, E. Furman, Q. M. Zhang, *Science* **2008**, 321, 821

[9] A. S. Mischenko, Q. Zhang, J. F. M. Scott, R. W. Whatmore, N. D. Mathur, *Science* **2006**, 311, 1270.

[10] X. Qian, H.-J. Ye, Y. Zhang, H. Gu, X. Li, C. A. Randall, Q. Zhang, *Adv. Funct. Mater.* **2014**, 24, 1300.

[11] R. Wang, S. Fang, Y. Xiao, E. Gao, N. Jiang, Y. Li, L. Mou, Y. Shen, W. Zhao, S. Li, A. F. Fonseca, D. S. Galv ã, M. Chen, W. He, K. Yu, H. Lu, X. Wang, D. Qian, A. E. Aliev, N. Li, C. S. Haines, Z. Liu, J. Mu, Z. Wang, S. Yin, M. c. D. Lima, B. An, X. Zhou, Z. Liu, R. H. Baughman, *Science* **2019**, 366, 216

[12] Y. Taguchi, H. Sakai, D. Choudhury, *Adv. Mater.* **2017**, 29 1606144.

[13] R. Ma, Z. Zhang, K. Tong, D. E. Huber, R. Kornbluh, Y. S. Ju, Q. Pei, *Science* **2017**, 357, 1130.

[14] Y. Bo, Q. Zhang, H. Cui, M. Wang, C. Zhang, W. He, X. Fan, Y. Lv, X. Fu, J. Liang, Y. Huang, R. Ma, Y. Chen, *Adv. Energy Mater.* **2021** 11, 2003771.

[15] Y. Meng, Z. Zhang, H. Wu, R. Wu, J. Wu, H. Wang, Q. Pei, *Nat. Energy* **2020**, 5, 996.

[16] Y. Wang, Z. Zhang, T. Usui, M. Benedict, S. Hirose, J. Lee, J. Kalb, D. E. Schwartz, *Science* **2020**, 370, 129.

[17] B. Nair, T. Usui, S. Crossley, S. Kurdi, G. G. Guzman-Verri, X. Moya, S. Hirose, N. D. Mathur, *Nature* **2019**, 575, 468.

[18] T. Alvar, P. Lheritier, T. Usui, Y. Nouchokgwe, M. Gerard, O. Bouton, S. Hirose, E. Defay, *Science* **2020**, 370, 125

[19] F. Le Goupil, K. Kallitsis, S. TencéGirault, N. Pouriamanesh, C. Brochon, i. Cloutet, T. Soulestin, F. Domingue Dos Santos, N. Stingelin, G. Hadziioannou, *Adv. Funct. Mater.* **2020**, 33, 2007043.

[20] X. Qian, D. Han, L. Zheng, J. Chen, M. Tyagi, Q. Li, F. Du, S. Zheng, X. Huang, S. Zhang, J. Shi, H. Huang, X. H. Shi, J. Chen, H. Qin, J. Bernholc, X. Chen, L. Chen, L. Hong, Q. M. Zhang, *Nature* **2021**, 600, 7890.

[21] G. Zhang, Q. Li, H. Gu, S. Jiang, K. Han, M. R. Gadinski, M. A. Haque, Q. Zhang, Q. Wang, *Adv. Mater.* **2015**, 27, 1450.

[22] G. Zhang, X. Zhang, T. Yang, Q. Li, L. Chen, S. Jiang, Q. Wang, ACS Nano **2015**, 9, 7164

[23] H. Cui, Q. Zhang, Y. Bo, P. Bai, M. Wang, C. Zhang, X. Qian, R. Ma, *Joule* **2022**, 6, 1.

[24] Q. Li, G. Zhang, X. Zhang, S. Jiang, Y. Zeng, Q. Wang, *Adv. Mater.* **2015**, 27 2236.

[25] Y. Chen, J. Qian, J. Yu, M. Guo, Q. Zhang, J. Jiang, Z. Shen, L.-q. Chen, Y. Shen, *Adv. Mater.* **2020**, 32, 1907927.

[26] J. Qian, R. Peng, Z. Shen, J. Jiang, F. Xue, T. Yang, L. Chen, Y. Shen, *Adv. Mater*. **2019,** 31, 1801949**.**

[27] L. Yang, L. Yang, X. Qian, C. M. Koo, Y. Hou, T. Zhang, Y. Zhou, M. Lin, J. Qiu, Q. Zhang, *Nano. Energy* **2016**, 22, 461.

[28] L. Engel, S. I. Kruk, J. Shklovsky, Y. Shacham-Diamand, S. Krylov, *J. Micromech. Microrng.* **2014**, 24, 125027.

[29] T. And, A. Petchsuk, *Macromolecules* **2002**, 35, 7678.

[30] G. Zhang, L. Weng, Z. Hu, Y. Liu, R. Bao, P. Zhao, H. Feng, N. Yang, M.-y. Li, S. Zhang, S. Jiang, Q. Wang, *Adv. Mater.* **2019**, 31 1806642,

[31] C. A. Grabowski, S. P. Fillery, H. Koerner, M. N. Tchoul, L. F. Drummy, C. W. Beier, R. L. Brutchey, M. F. Durstock, R. A. Vaia, *Nanocomposites* **2016**, 2, 117.

[32] Q. Wang, L. Zhu, *J. Polym. Sci. Pol. Phys.* **2011**, 49, 1421.

[33] A. Jeowski, J. Mucha, R. Pazik, W. Strek, *Appl. Phys. Lett.* **2007**, 90, 11.

[34] S. Kar-Narayan, N. P. Mathur, *Appl. Phys. Lett. **2009**, 95, 242903.*

[35] Y. Meng, J. Pu, Q. Pei, *joule* **2021**, 5, 780.

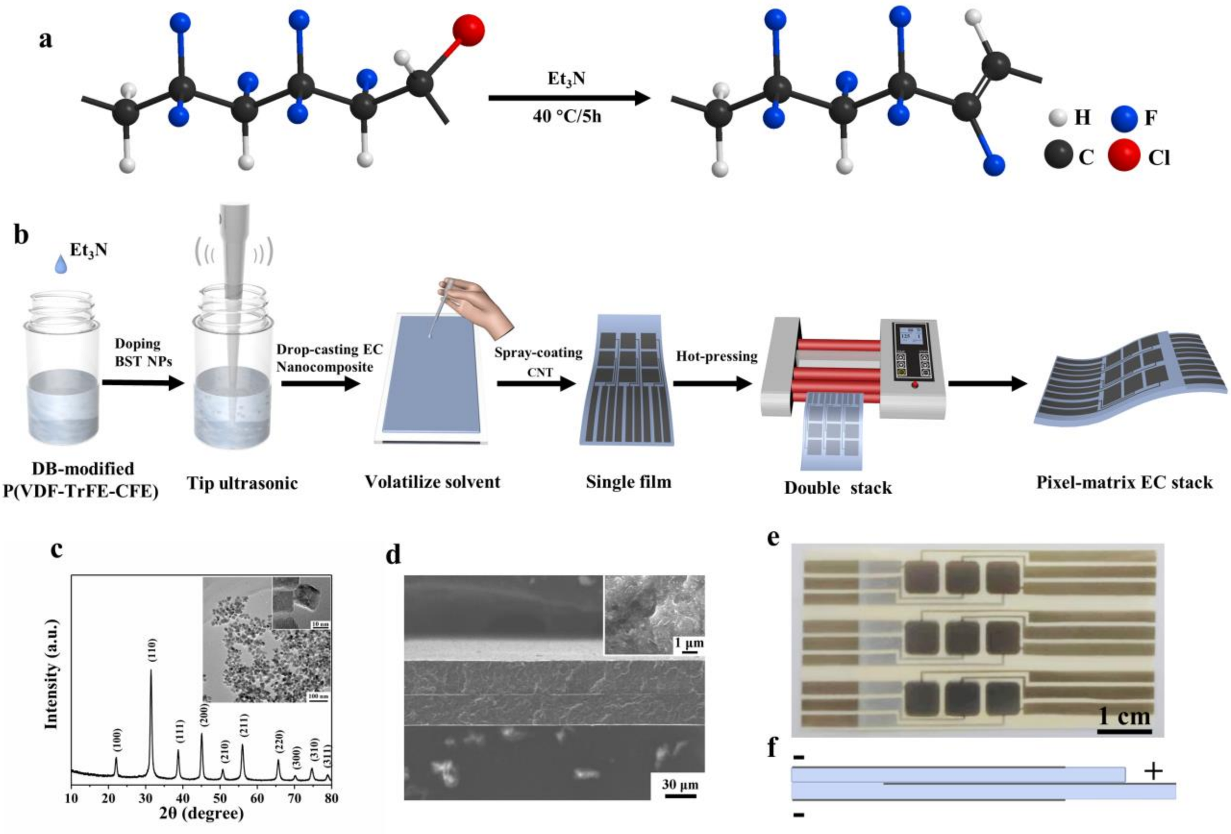

Figure 1. Preparation of pixel-matrix EC polymer nanocomposite stack. a) Schematic diagram of the de-hydrochlorination process to form double bonds in P(VDF-TrFE-CFE). b) Schematic of fabrication process of the pixel-matrix EC polymer nanocomposite stack. c) XRD pattern of BST NPs, the inset shows the TEM morphology of BST NPs. d) Cross-sectional SEM image of EC polymer nanocomposite stack, the inset shows the microstructure of BST NPs dispersed in the polymer matrix. e) Photographs of the pixel-matrix EC polymer nanocomposite stack, each active area is independent with the size of 6.5 mm×6.5 mm. f) Side view of EC nanocomposite stack.

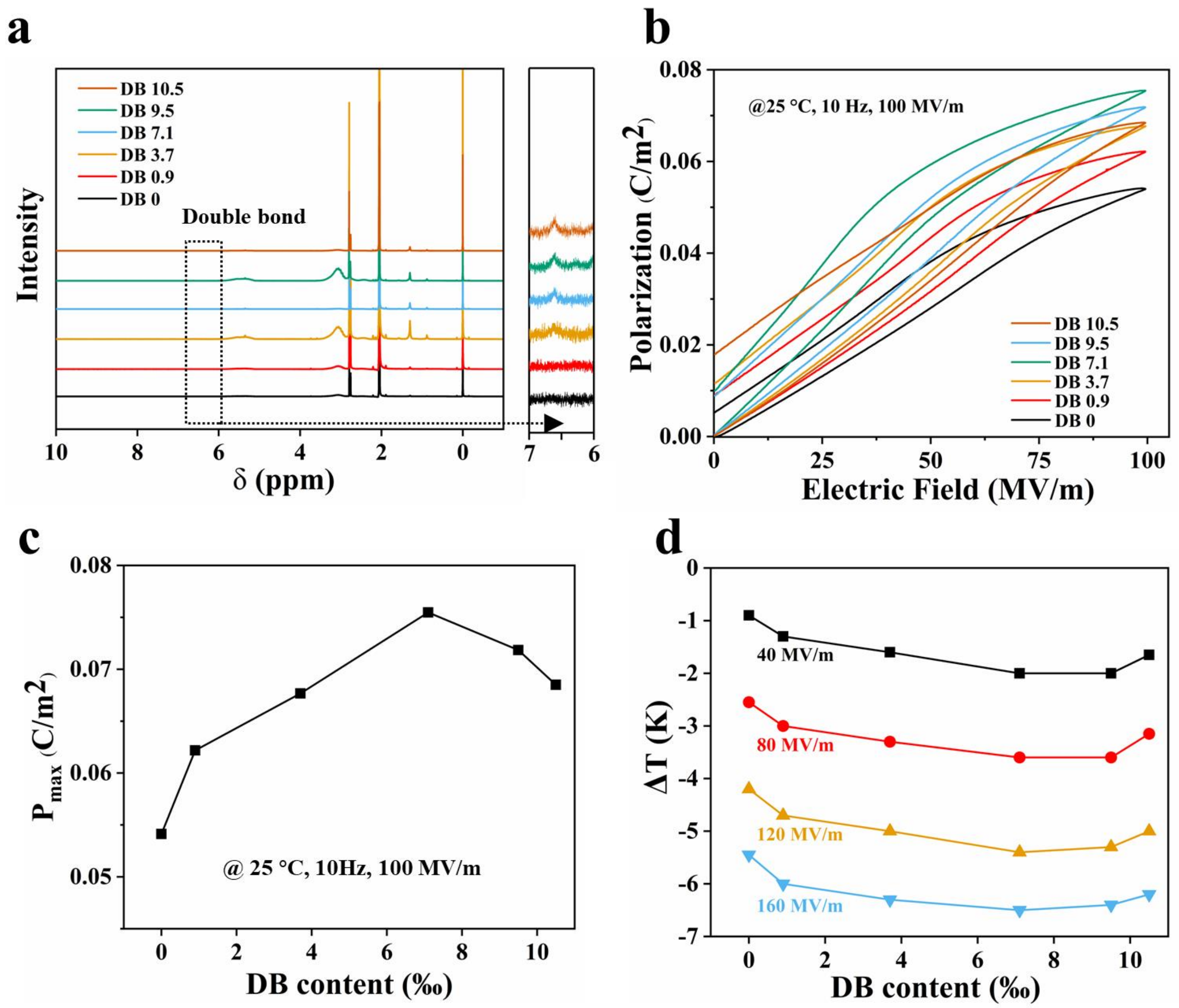

Figure 2. Performance of DB-modified P(VDF-TrFE-CFE). a) ^{1}H-NMR spectra of DB-modified P(VDF-TrFE-CFE) with different Et_3N content. b) Polarization-electric field loops (P-E loops) for DB-modified P(VDF-TrFE-CFE) at 10 Hz. c) Maximum polarization of DB-modified P(VDF-TrFE-CFE) as a function of DB content. d) Temperature change (ΔT) for DB-modified P(VDF-TrFE-CFE) under different electric fields at room temperature.

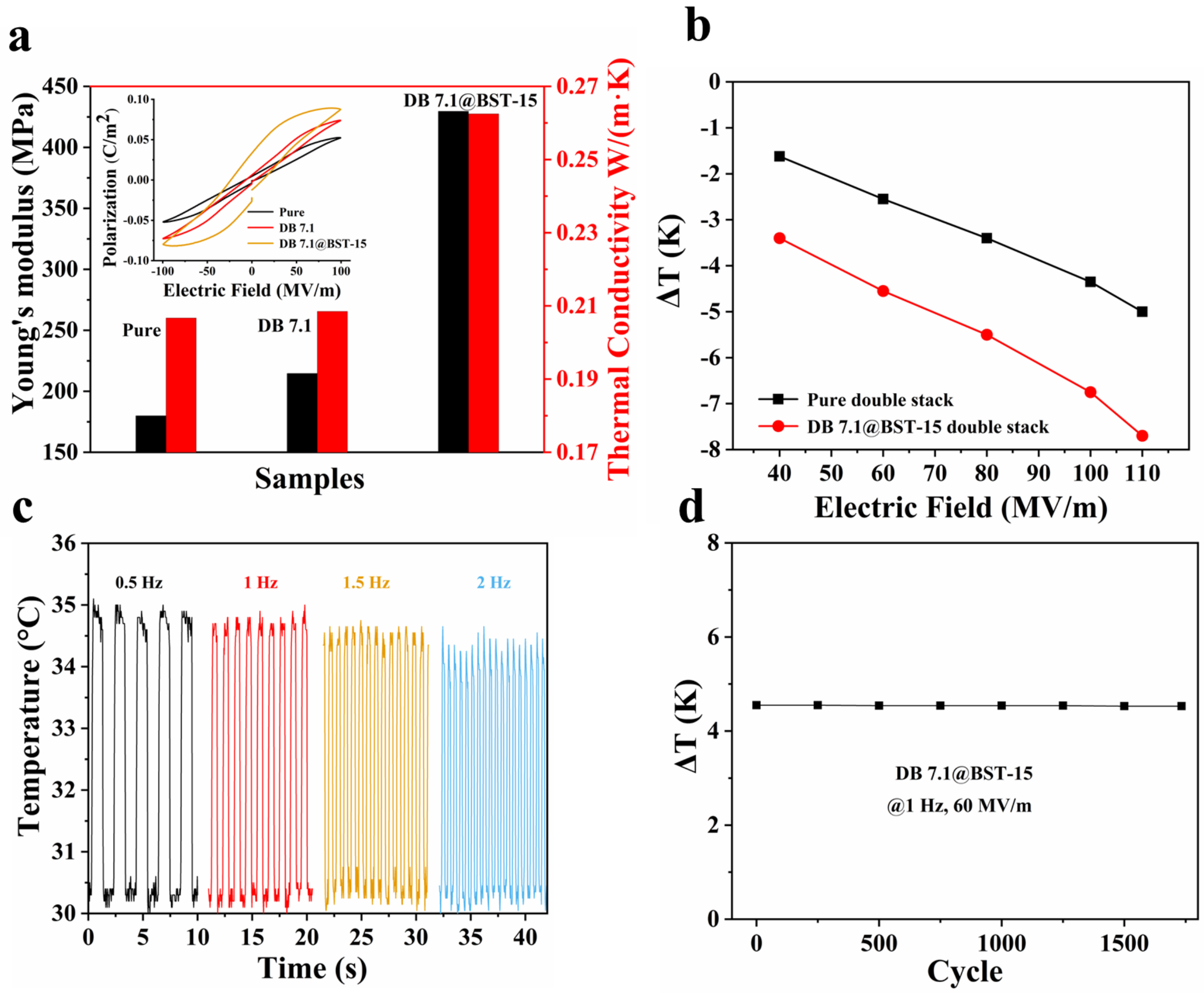

Figure 3. Performance of EC polymer nanocomposite stack. a) Young's modulus and thermal conductivity of the pure P(VDF-TrFE-CFE), DB 7.1, and DB 7.1@BST-15. The inset shows P–E loops of pure P(VDF-TrFE-CFE), DB 7.1, and DB 7.1@BST-15 under the electric field of 100 MV/m. b) ΔT of two-layer P(VDF-TrFE-CFE) stack and two-layer DB 7.1@BST-15 stack. c) ΔT of two-layer DB 7.1@BST-15 stack under 60 MV/m with different frequencies. d) Cyclic stability test of two-layer DB 7.1@BST-15 stack with the operating frequency of 1 Hz at 60 MV/m.

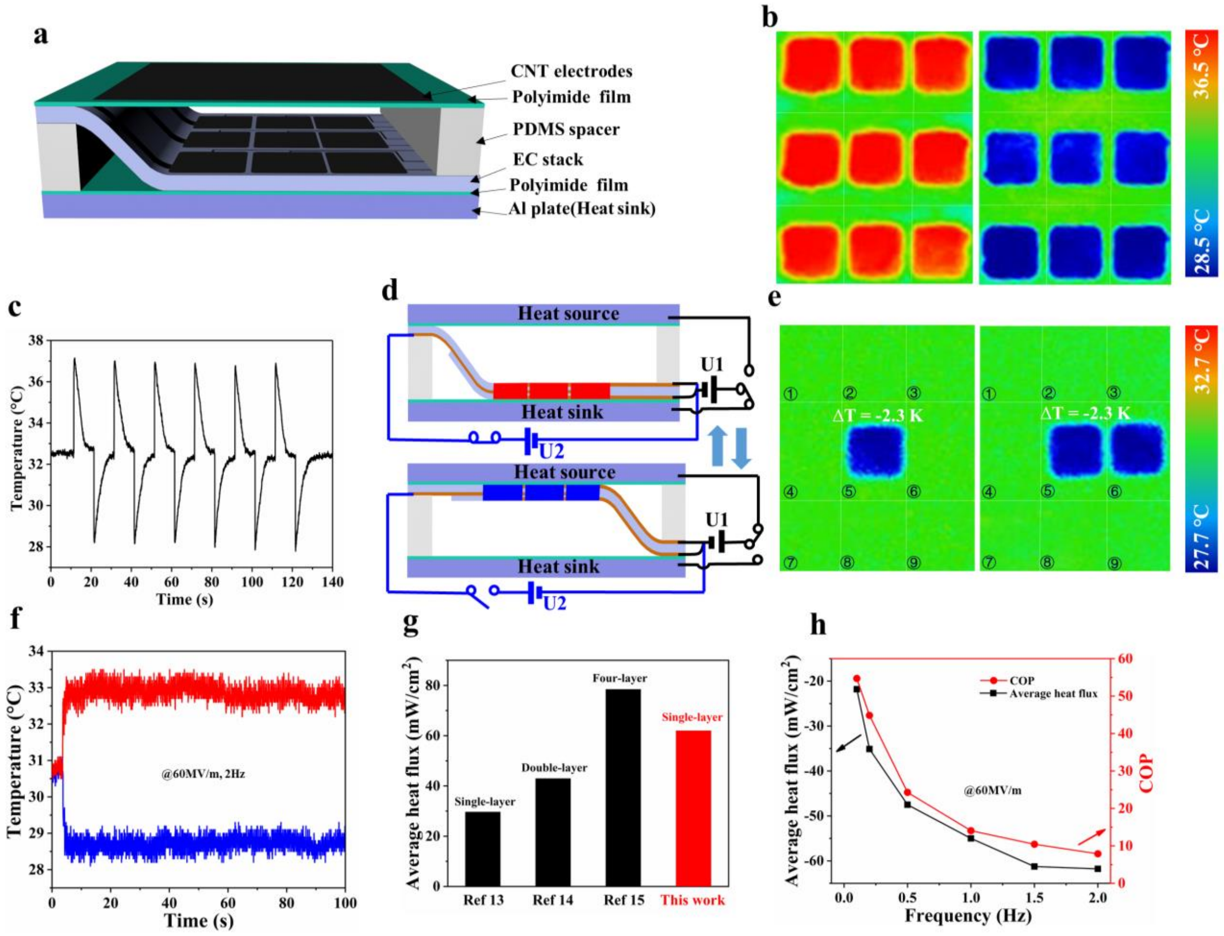

Figure 4. The pixel-matrix EC cooling device and its operational mechanism. a) Schematic illustration of pixel-matrix EC cooling device. b) Infrared images of an EC nanocomposite stack with a 3 × 3 electrode matrix, when an electric field of 60 MV/m is applied (left) and removed (right). c) Time–temperature profile of EC nanocomposite stack with application and removal of a 60 MV/m electric field at a 0.05 Hz frequency. d) Schematic illustration of a pixel-matrix EC cooling device showing how heat is continually pumped from heat source to heat sink by an alternating electrostatic force, along with a repeated charging-discharging process for EC effect.[13] e) Infrared images of pixel-matrix EC cooling device with one active pixel (left) and two active pixels (right). f), Temperature span

of an active pixel in pixel-matrix EC cooling device under electric field of 60 MV/m at a frequency of 2 Hz. g) Comparison of average heat flux of different EC cooling devices. h) Average heat flux and COP of the pixel-matrix EC cooling device as a function of the operating frequency under the electric field of 60 MV/m.

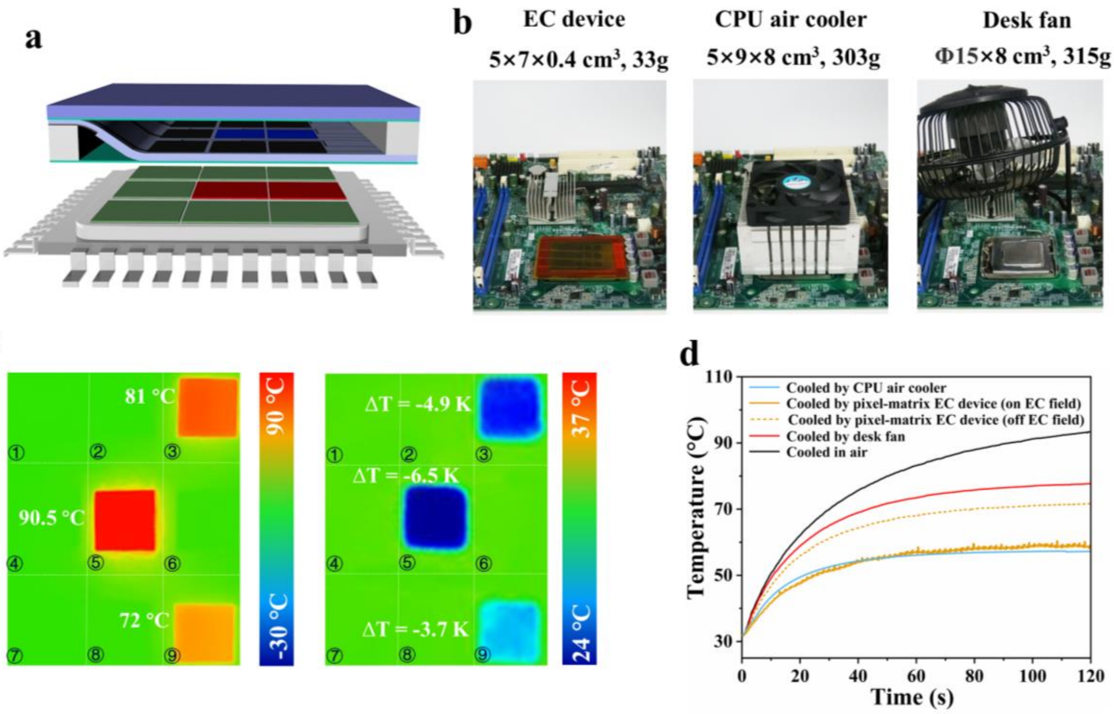

Figure 5. Demonstration of the potential application of targeted and differential thermal management in microelectronics. a) Schematic illustration of the pixel-matrix EC cooling device for targeted and differential thermal management aiming to CPU with localized overheating. b) Size comparison of our pixel-matrix EC cooling device, CPU air cooler and desk fan. c) Infrared images of a 3 × 3-pixel simulated CPU with uneven temperature distribution (left) and the pixel-matrix EC nanocomposite stack with three activated active pixels (right). d) Time-resolved temperature curves of simulated CPU cooled in air (black),

by desk fan (red), by cooling fin with fan (cyan), and by the pixel-matrix EC cooling device (brown).

We demonstrate a highly efficient pixel-matrix electrocaloric cooling device on which each refrigeration pixel can be independently controlled, and can effectively cool down the localized overheating on microelectronics in situ as needed. All active pixels in the EC cooling device exhibit a stable temperature span of 4.6 K and a heat flux of 62 mW/cm.

Peijia Bai, Quan Zhang, Heng Cui, Yiwen Bo, Ding Zhang, Wen He, Yongsheng Chen, Rujun Ma*

An active pixel-matrix electrocaloric device for targeted and differential thermal management